ELSEVIER

J. Non-Newtonian Fluid Mech. 110 (2003) 45–75

Journal of Non-Newtonian Fluid Mechanics

www.elsevier.com/locate/jnnfm

Benchmark solutions for the flow of Oldroyd-B and PTT fluids in planar contractions

Manuel A. Alves [a], Paulo J. Oliveira [b,*], Fernando T. Pinho [c]

[a] *Departamento de Engenharia Química, CEFT, Faculdade de Engenharia da Universidade do Porto, Rua Dr. Roberto Frias, 4200-465 Porto, Portugal*

[b] *Departamento de Engenharia Electromecânica, Universidade da Beira Interior, Rua Marques D'Avila e Bolama, 6201-001 Covilhã, Portugal*

[c] *Centro de Estudos de Fenómenos de Transporte, DEMEGI, Faculdade de Engenharia da Universidade do Porto, 4200-465 Porto, Portugal*

Received 20 July 2002; received in revised form 8 December 2002

Abstract

The paper presents very accurate numerical results for the vortex size, the vortex intensity and the Couette correction, in planar contraction flows of Oldroyd-B and PTT fluids ($\varepsilon = 0.25$) with both the linear and the exponential stress function, and with a solvent viscosity ratio equal to 1/9. The accuracy of these results is quantified, being generally below 1% (0.3% for most results), and the finest mesh employed had over 1 million degrees of freedom. Such degree of mesh fineness is shown to be required for accurate results with the Oldroyd-B fluid, especially at high Deborah numbers, but the shear-thinning PTT fluid in general does not require the finest meshes. In terms of level of elasticity, steady results for the PTT fluid could be obtained for values of the Deborah number in excess of 100 (linear PTT) and 10,000 (exponential PTT).

Keywords: Benchmark results; Plane contraction; Oldroyd-B; PTT; Viscoelastic fluid; Couette correction

1. Introduction

In computational rheology there are a number of flow problems often used as test cases for the development of new numerical methods and assessment of their accuracy. Examples are the viscoelastic flow through axisymmetric and planar contractions, flow around cylinders or spheres, either confined or unconfined, flow through corrugated channels, stick-slip flows, and some others (cf. [1,2]). While for some of these test cases quantitative results are either tabulated or given under the form of graphs from where data can be extracted and used for comparison by other researchers, for other cases such data have

* Corresponding author. Fax: +351-275-329972/320820.
E-mail addresses: mmalves@fe.up.pt (M.A. Alves), pjpo@ubi.pt (P.J. Oliveira), fpinho@fe.up.pt (F.T. Pinho).

0377-0257/03/$ – see front matter © 2003 Elsevier Science B.V. All rights reserved.
doi:10.1016/S0377-0257(02)00191-X

never been provided quantitatively and comparison can be qualitative at best. Example of the former situation is the drag coefficient for low Reynolds number flow around either spheres (see a comparison of various results in [2]) or cylinders (excellent agreement between [3] and [4]), all given by numerical investigations; those data are then used to demonstrate that different methods yield results in close agreement, hence imparting confidence on the solutions and the methods. For other problems, typified here by planar contraction flows, such quantitative data are either missing or have only recently been provided [5–8], but still without a clear indication of the expected range of validity [5,7,8]. It is true that the flow through abrupt contractions gives rise to a singularity at the re-entrant corner located at the entrance to the smaller duct, where stresses tend to infinity thus posing severe difficulties to the numerical methods and the pursue of accurate solutions.

It is the purpose of the present work to provide quantitative data of benchmark quality for the inertialess flow through a 4:1 planar contraction of viscoelastic liquids obeying either the constant viscosity Oldroyd-B constitutive model, or the shear-thinning PTT model with linear or exponential stress functions. The data given comprises the size of the corner vortex formed upstream of the contraction, its intensity in terms of entrapped flow rate, the pressure drop through the contraction, longitudinal profiles of velocity and normal stress along the centreline, and asymptotic variation of velocity and stresses near the singular re-entrant corner. The accuracy of these global data is assessed in a precise manner, by comparison with extrapolated values therefore providing a quantitative error estimate, and in a less precise manner by comparison between predictions on various computational meshes. A finite-volume numerical method was used to obtain these results and the accuracy of the different schemes utilised to represent the spatial derivatives in the governing equations is demonstrated to be second order at least. Consistent mesh refinement has been carried out on six consecutively refined meshes, the finest of which has over 1 million degrees of freedom. The computational code employed here is essentially the same of [4], where excellent agreement has been demonstrated with the independent predictions of [3] for the viscoelastic flow around a confined cylinder.

Of the two types of sudden contraction flow geometries, the one that has received more attention, both numerically and experimentally, is the axisymmetric configuration. The planar configuration, on the other hand, is better suited to visualisation studies through birefringence strand techniques, as in the works [9–11], and is equally relevant to engineering flows in extrusion dies. In a previous paper [12], we have reviewed the published numerical work on planar contraction flows and have provided numerical solutions based on the upwind scheme but using very refined meshes. Later [6], we published accurate results for the case of the flow of an upper convected Maxwell (UCM) fluid, giving special attention to issues of accuracy and mesh refinement, particularly to the effects brought about by improved numerical spatial discretisations in contrast to plain upwind differencing. Amongst the more recent computational work we emphasise that of Aboubacar and Webster [7] and Aboubacar et al. [8] who have done a very comprehensive study of Oldroyd-B and PTT fluids flowing through sharp and rounded-corner planar contractions, having highlighted the influence of the fluids Trouton ratio on the vortex patterns. Although the conclusions of these authors regarding flow behaviour in planar contractions are indisputably correct, as we shall show their data still lack the degree of accuracy required for benchmark data and that is the gap we would like to fulfil with this work.

To illustrate from the outset the level of scatter of the numerical data from the literature for this problem, we plot in Fig. 1(a) existing data for the size of the recirculating corner vortex (X_R, normalised with half-width of smaller channel) and in Fig. 1(b) predictions of the vortex intensity (Ψ_R, normalised with inlet flow rate). Both these quantities are plotted as a function of elasticity level, measured by a

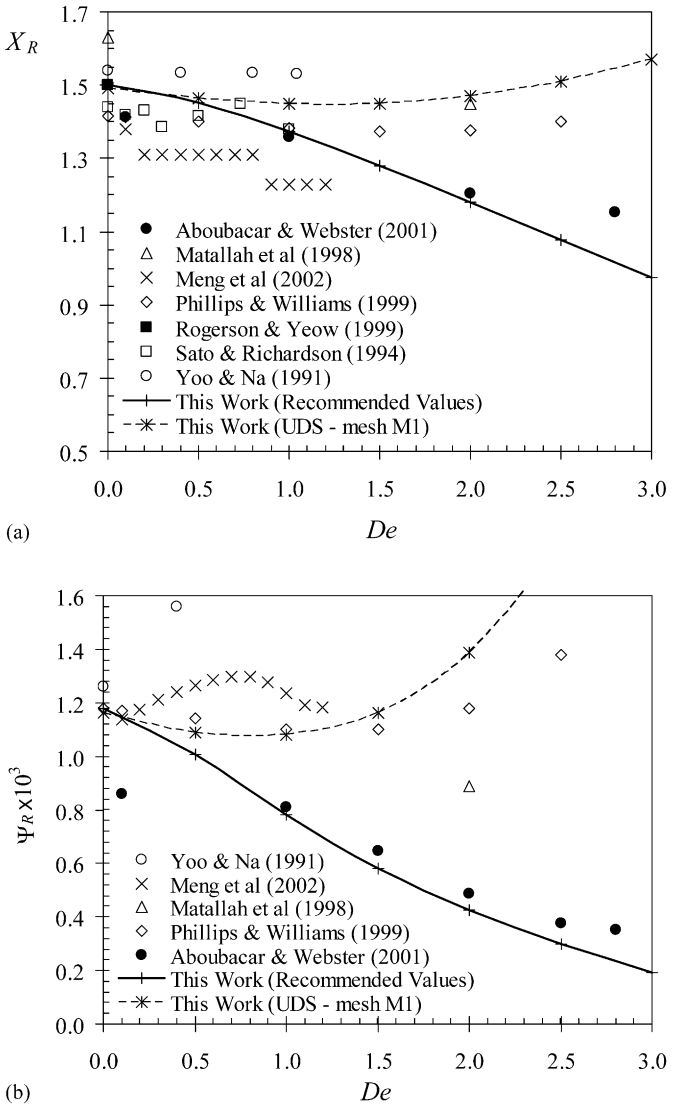

Fig. 1. Present status in published values for the corner vortex characteristics with the Oldroyd-B fluid in a 4:1 planar contraction: (a) size; (b) intensity.

Deborah number $De = \lambda U_2/H_2$, and pertain to the Oldroyd-B fluid. There is clearly too much dispersion in these results and trends in data are not even consistent. Obviously, some degree of convergence, in terms of accuracy, is required if the planar contraction flow is to remain one of the benchmark problems in non-Newtonian viscoelastic computations. In these figures, we also show the outcome from the present study (solid lines), and also some numerical results obtained on a coarse mesh with the upwind scheme (dashed lines), in order to illustrate the type of disparity between accurate and less accurate solutions. Further discussion is given in Section 4.

We believe that the results of the current study will provide a definite answer to some of the discrepancies seen in Fig. 1 and they will be very useful for others, as a check of their codes in this relevant problem of relative geometrical simplicity. We would like to emphasise that even for Newtonian fluids it has been extremely difficult to find reliable data for the creeping flows of interest here.

In Section 2 the governing equations are given and the numerical method described in broad terms. The geometry and computational meshes are defined in Section 3. The results for the Oldroyd-B, linear PTT and exponential PTT fluids are given and discussed in Sections 4–6, respectively.

2. Governing equations and numerical method

The equations governing the laminar flow of an incompressible viscoelastic fluid are those expressing conservation of mass:

$$\nabla \cdot \boldsymbol{u} = 0, \tag{1}$$

and momentum:

$$\rho \left[\frac{\partial \boldsymbol{u}}{\partial t} + \nabla \cdot \boldsymbol{u}\boldsymbol{u} \right] = -\nabla p + \eta_s \nabla \cdot \nabla \boldsymbol{u} + \nabla \cdot \boldsymbol{\tau}, \tag{2}$$

together with a constitutive relation for the extra, elastic part of the stress tensor $\boldsymbol{\tau}$, here taken as a differential equation:

$$\lambda \left[\frac{\partial \boldsymbol{\tau}}{\partial t} + \nabla \cdot \boldsymbol{u}\boldsymbol{\tau} \right] + f(\mathrm{Tr}\,\boldsymbol{\tau})\boldsymbol{\tau} = \eta_p(\nabla \boldsymbol{u} + \nabla \boldsymbol{u}^{\mathrm{T}}) + \lambda(\boldsymbol{\tau} \cdot \nabla \boldsymbol{u} + \nabla \boldsymbol{u}^{\mathrm{T}} \cdot \boldsymbol{\tau}). \tag{3}$$

The last equation represents a simplified form of the PTT model [13,14] where only the upper convected part of the full Gordon–Schowalter derivative is retained. The stress function $f(\mathrm{Tr}\,\boldsymbol{\tau})$ may follow either the linear form proposed in the original work [13]:

$$f(\mathrm{Tr}\,\boldsymbol{\tau}) = 1 + \frac{\lambda\varepsilon}{\eta_p}\,\mathrm{Tr}(\boldsymbol{\tau}), \tag{4}$$

or the exponential form proposed later by Phan-Thien [14]:

$$f(\mathrm{Tr}\,\boldsymbol{\tau}) = \exp\left[\frac{\lambda\varepsilon}{\eta_p}\,\mathrm{Tr}(\boldsymbol{\tau}) \right]. \tag{5}$$

In Eqs. (2)–(5), the constant model parameters are the relaxation time λ, the zero-shear polymer viscosity η_p, the solvent viscosity η_s, and the extensibility parameter ε. If ε is set to zero, this constitutive model becomes identical to the Oldroyd-B equation where the ratio between the solvent viscosity and the total viscosity is $\beta = \eta_s/\eta_0$, with $\eta_0 = \eta_s + \eta_p$. In the current work, β is taken as $\beta = 1/9$ in accordance with many previous studies.

A fully-implicit finite-volume method is used to solve Eqs. (1)–(3). It is based on a time marching pressure-correction algorithm formulated with the collocated variable arrangement, as explained in detail in [15]. The governing equations are integrated in space over the control volumes (cells, with volume

V_P) forming the computational mesh, and in time over a time step (δt), so that sets of linearised algebraic equations are obtained, having the general form:

$$a_P \boldsymbol{u}_P = \sum_{F=1}^{6} a_F \boldsymbol{u}_F + \boldsymbol{S}_{\boldsymbol{u}}, \tag{6}$$

to be solved for the velocity components, and

$$a_P^{\boldsymbol{\tau}} \boldsymbol{\tau}_P = \sum_{F=1}^{6} a_F^{\boldsymbol{\tau}} \boldsymbol{\tau}_F + \boldsymbol{S}_{\boldsymbol{\tau}}, \tag{7}$$

to be solved for the extra stress components. In these equations, a_F are coefficients, accounting for convection and diffusion influences, $\boldsymbol{S}$ are source terms encompassing all contributions not included in the coefficients, the index P denotes the cell at the centre of the computational molecule and F the corresponding neighbouring cells. The central coefficient of the momentum equation is given by:

$$a_P = \frac{\rho V_P}{\delta t} + \sum_{F=1}^{6} a_F, \tag{8}$$

where the first term arises from the time-dependent term in the original equation and is used here with the purpose of inertial under-relaxation since the interest is only in steady state solutions. Similarly, the central coefficient of the stress equation for the linear PTT model is given by:

$$a_P^{\boldsymbol{\tau}} = \frac{\lambda V_P}{\delta t} + V_P \left(1 + \frac{\lambda \varepsilon}{\eta_p} \mathrm{Tr}(\boldsymbol{\tau}_P)\right) + \sum_{F=1}^{6} a_F^{\boldsymbol{\tau}}, \tag{9}$$

and for the exponential PTT model it suffices to replace the term in brackets by the exponential stress function (Eq. (5)). It is important to notice that the effect brought about by the PTT model, compared with the UCM, is to increase the central coefficient (since $\mathrm{Tr}(\boldsymbol{\tau})$ is always positive and usually large) and thus promoting numerical stability.

After having assembled the coefficients and source terms, the linear sets of Eq. (6) are sequentially solved for the two Cartesian velocity components u and v, by means of a preconditioned bi-conjugate gradient solver. These newly computed velocity components will not, in general, satisfy the continuity equation (Eq. (1)) and need therefore to be corrected by adjustment of the pressure differences which drive them. This is accomplished by means of a pressure-correction field obtained from a pressure Poisson equation, derived from the discretised equivalent of (1) and a simplified form of (6), which is then solved with a symmetric conjugate gradient method. Once we are in possession of a continuity-satisfying velocity field, we may solve sequentially the implicitly-discretised constitutive equations for τ_{xx}, τ_{yy} and τ_{xy} (Eq. (7)); the same bi-conjugate solver is employed for this purpose. Note that the source term $\boldsymbol{S}_{\boldsymbol{u}}$ in (6) depends on the stress field, and the source term $\boldsymbol{S}_{\boldsymbol{\tau}}$ in (7) depends on the velocity field; the time advancement of the equations thus acts as an iterative procedure with the time step playing the role of an equivalent under-relaxation factor.

Most importantly for accuracy is the representation of the convective terms in the constitutive equations. The base scheme we consider is an upwind differencing scheme (UDS) in which a cell face stress is given by the corresponding cell centre value in the upstream direction, and the contribution of those upwind

fluxes are included in the coefficients. This scheme leads to too much numerical diffusion, a fact known for a long time in Newtonian CFD and for almost a decade by the non-Newtonian community. Yet, upwind is still used by some research groups, especially with finite-volume methods, but clearly better stress convection schemes are required, especially to deal with elastic flow predictions. The constitutive equations are of the hyperbolic type, without any physical diffusion term, and high order schemes must be accompanied by high-resolution or TVD type of restrictions in order to dampen the formation of any numerical oscillations in regions of high gradients. A new convection scheme especially designed for differential constitutive relations has been proposed in [16] and it is here adopted throughout. It has the advantage over more classical schemes, like the SMART scheme of Gaskell and Lau [17], of promoting iterative convergence when employed in conjunction with implicit methods.

3. Geometry and computational meshes

A sketch of the contraction geometry is given in Fig. 2. Only half of the two-dimensional domain is used for the computations, with symmetry conditions imposed at the centreline, $y = 0$. We are therefore unable to capture possible flow bifurcations resulting in asymmetric vortical structures. The half-width of the shorter channel H_2 is taken as the characteristic length scale and the average velocity in that channel U_2 is the characteristic velocity scale. Stress and pressure are normalised with $\eta_0 U_2/H_2$ (often, to be consistent with previous work, we use the scaling $\tau_{w,0} \equiv 3\eta_0 U_2/H_2$ for the stresses). Due to the very high elasticity attained in the present calculations, longer inlet and outlet channel lengths have been assumed as base values, compared with our previous studies [6,12]. Here we took an inlet length $L_1 = 40H_2$ and an outlet length $L_2 = 100H_2$. These lengths are required for complete flow development upstream of the contraction, and complete flow redevelopment downstream of it; although fully developed flow at inlet and outlet is not a requirement to obtain precise vortex data, it is a requirement to obtain precise values of Couette correction (non-dimensional pressure loss). For the highest elastic cases, L_2 was even longer than the base value; this is discussed in Sections 5 and 6.

The mesh data in Table 1 comprise the total number of control volumes in the meshes (NC), the degrees of freedom (DOF) and the minimum mesh spacing normalised with H_2. Fig. 10, to be discussed later, gives a zoomed view of a small portion of mesh M6 near the re-entrant corner; as expected, the smallest cells are clustered around the corner and their size expands very smoothly as one moves away from the singular point. M6 is an extremely refined mesh, with significant mesh concentration not only around

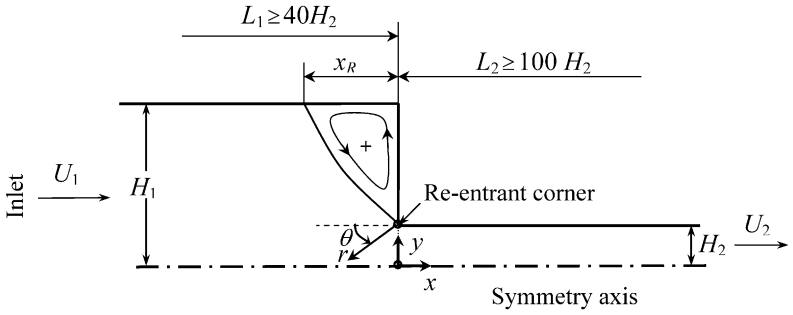

Fig. 2. Sketch of the contraction geometry.

Table 1
Major characteristics of the computational meshes

Mesh	NC	DOF	$\Delta x_{min} = \Delta y_{min}$
M1	5282	31692	0.020
M2	10587	63522	0.014
M3	21128	126768	0.010
M4	42348	254088	0.0071
M5	84512	507072	0.0050
M6	169392	1016352	0.0035

NC: number of cells; DOF: degrees of freedom; Δx, Δy: cell spacing.

the re-entrant corner and downstream channel wall, but also in the upstream wall region where mesh refinement is useful to resolve accurately the main features of the corner vortex.

A large number of computations have been performed on the meshes defined in Table 1, for increasing values of the Deborah number $De \equiv \lambda U_2/H_2$ but for a constant vanishing Reynolds number $Re \equiv \rho U_2 H_2/\eta_0 = 0$, so as to allow comparison with existing results. For both the Oldroyd-B and PTT models, the viscosity ratio was kept constant at the often used value $\beta = 1/9$, and the value assigned to the extensional parameter of the PTT was $\varepsilon = 0.25$, typical of polymer melts. Furthermore, the two forms of the PTT model were considered: linear and exponential stress functions.

The results of all these computations may be divided into two classes: qualitative and quantitative. The qualitative results to be given essentially comprise streamline plots, an effective way of illustrating the effect of elasticity on vortex enhancement and checking the existence or not of lip vortices. The main contribution of the work is however the quantitative results, which comprise tables and figures for the size of the corner vortex X_R, intensity of the corner vortex Ψ_R, intensity of lip vortex (when present) Ψ_L, entry pressure drop expressed as a Couette correction coefficient $C \equiv (\Delta p - \Delta p_{fd})/2\tau_w$, and maximum values of normal stress and axial velocity along the centreline of the channels. In the Couette correction, τ_w is the wall shear stress for the fluid in question (encompassing both the solvent and the polymer contributions) evaluated under fully developed conditions in the smaller channel. The uncertainty of these data is quantified by means of the Richardson extrapolation technique.

Results are first given for the Oldroyd-B fluid (Section 4), and then for the linear and exponential forms of the PTT fluid (Sections 5 and 6). When of interest, results for the different fluids are compared.

4. Results for the Oldroyd-B fluid

Results for the vortex size and intensity, and for the pressure drop of the Oldroyd-B fluid with $\beta = 1/9$, obtained on the three successively refined meshes M2, M4 and M6 generated by halving the mesh space, are presented in Figs. 3–5 and in Table 2. All these quantities are seen to decrease with elasticity, measured by the Deborah number, up to a level of $De \approx 3$. Convergence could not be achieved for the higher value of De on the finest mesh M6 and so it is not possible to answer the question of whether vortex activity would eventually increase at higher elasticity, as was the case for the UCM predictions in [6,12]. The "Percent error" in Tables 2–4 quantify the relative difference between the predictions on the finest mesh and the extrapolated results obtained from Richardson's extrapolation technique. They are a measure of the uncertainty of our results. It is worth noting that the benchmark data given in the tables are our "best"

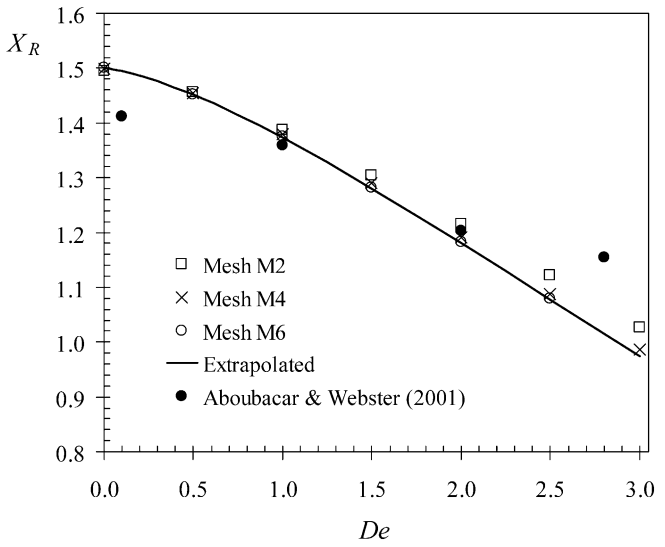

Fig. 3. Variation of the vortex size X_R with the Deborah number *De* for the Oldroyd-B fluid.

(more accurate) results based on Richardson's extrapolation to the limit. On the first meshes (M1 and M2) we could attain higher *De*-values but the corresponding data are not given in the tables.

For the purpose of comparison with data for X_R and Ψ_R reported in the literature, which were discussed in Section 1 in relation to Fig. 1, we have also carried out computations with the low-accuracy upwind scheme on our coarsest mesh M1. These predictions are plotted in Fig. 1(a) and (b), respectively, as dashed lines; they lie in the middle of the scatter represented by the existing data, implying poor resolution inherent to most of these.

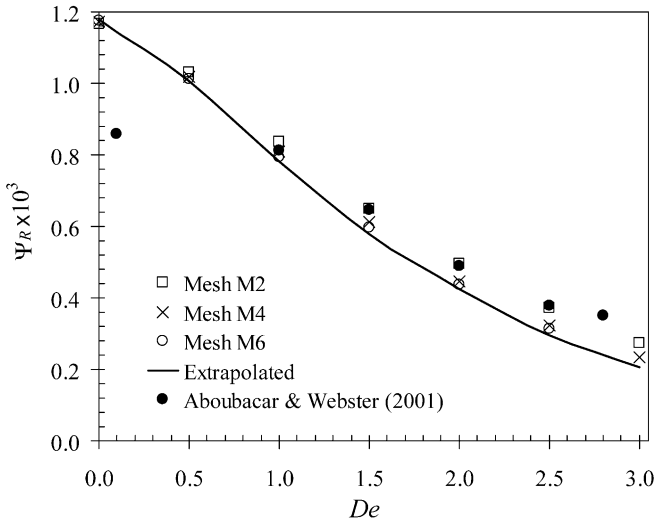

Fig. 4. Variation of the corner vortex intensity Ψ_R with the Deborah number *De* for the Oldroyd-B fluid.

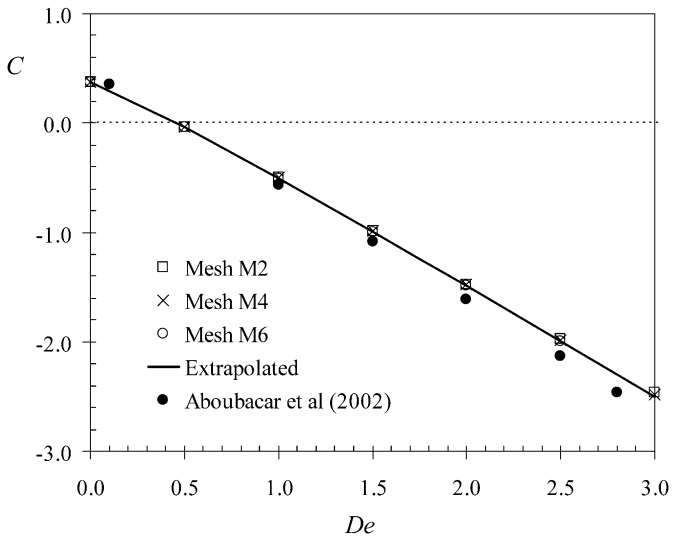

Fig. 5. Variation of the Couette correction C with the Deborah number De for the Oldroyd-B fluid.

It is also pertinent to note that although the Couette correction is not too sensitive to mesh refinement, the vortex characteristics X_R and Ψ_R vary in a discernible way amongst the three meshes, especially as De is increased; at $De = 3$ there is a variation of 0.7% in X_R and 3.1% in Ψ_R when going from mesh M4 to M5. The errors in Ψ_R seen in Table 2, and in the remaining tables for the PTT fluids, are usually greater than the errors for X_R and C; this is because Ψ_R requires integration of the velocity field, therefore lowering the convergence rate (see comments in [6], p. 303).

For comparison purposes we include in the above figures the recent data of Aboubacar and Webster [7], obtained with a hybrid finite-volume/element method on a mesh with a minimum spacing of 0.011 (it is not clear if this corresponds to our Δx_{min}) and 32,717 DOF. The results of these authors coincide with ours on our coarse mesh M2, except for the higher De where the deviation may be explained by onset of numerical divergence, and also for the lower $De = 0.1$. When De tends to zero the results should tend to the Newtonian solution. A recent semi-analytic study of creeping flow by Rogerson and Yeow [18] gave

Table 2
Benchmark results for the Oldroyd-B model with $\beta = 1/9$

De	X_R	Percent error	$\Psi_R \times 10^3$	Percent error	C	Percent error	$\tau_{xx,max}$ [a]	u_{max} [a]
0.0	1.5002	0.02	1.178	0.2	0.3741	0.1	0.360	1.501
0.5	1.4520	0.02	1.006	0.6	−0.0360	1.0	0.461	1.511
1.0	1.373	0.1	0.780	2.0	−0.505	0.4	0.544	1.525
1.5	1.279	0.2	0.576	3.0	−0.995	0.4	0.589	1.537
2.0	1.181	0.2	0.422	4.0	−1.492	0.3	0.612	1.546
2.5	1.077	0.3	0.297	6.0	−1.996	0.4	0.623	1.554
3.0[b]	0.973	0.6	0.207	9.0	−2.501	0.7	0.638	1.562

[a] Maximum values along centreline, normalised with $3\eta_0 U_2/H_2$ and U_2.
[b] Based on the results obtained with meshes M1–M5.

Table 3
Benchmark results for the linear PTT with $\varepsilon = 0.25$

De	X_R	Percent error	$\Psi_R \times 10^3$	Percent error	C	Percent error	$\tau_{xx,max}$ [a]	u_{max} [a]
0.0	1.5002	0.02	1.178	0.2	0.3741	0.1	–	1.501
0.1	1.500	0.1	1.178	0.2	0.3092	0.1	0.349	1.495
0.2	1.501	0.1	1.179	0.2	0.2581	0.2	0.368	1.484
0.5	1.506	0.1	1.201	0.1	0.1672	0.2	0.399	1.465
1	1.542	0.1	1.339	0.1	0.0951	0.3	0.415	1.468
2	1.639	0.1	1.781	0.1	0.0261	1.0	0.405	1.484
5	1.898	0.1	3.31	0.5	−0.0551	0.9	0.340	1.512
10	2.131	0.1	4.76	0.7	−0.1113	0.6	0.264	1.531
20	2.321	0.1	5.73	1.0	−0.1460	0.3	0.183	1.542
50	2.493	0.2	6.34	2.0	−0.1444	0.4	0.0920	1.544
100	2.57	0.5	6.48	2.0	−0.0917	1.0	0.0480	1.540

[a] Maximum values along centreline, normalised with $3\eta_0 U_2/H_2$ and U_2.

$X_R \approx 1.5$ which coincide with our result in Fig. 3. From private communications with Prof. M.F. Webster, it is plausible that the deviation at low De seen in Figs. 3 and 4 (and in the corresponding figures for the PTT fluids to be shown later) might be caused by insufficient time stepping in the computations of [7,8], hence leading to a too loose iterative convergence stopping-criterium. This could be expected, since the time scale for the viscoelastic flow can be taken as proportional to the relaxation time of the fluid, with a time step chosen accordingly, whereas the time scale for the Newtonian flow is a characteristic diffusion time $\propto \rho H_2^2/\eta_0$ which is very small. As a consequence, when $De \to 0$ the δt used in the computations becomes small and many time steps will be required to reach a single unit relaxation time.

Fig. 6 demonstrates the quadratic convergence of the present discretisation schemes, viewed as a whole (for convection, diffusion and sources), even for the large Deborah number case shown ($De = 2.5$). Values

Table 4
Benchmark results for the exponential PTT with $\varepsilon = 0.25$

De	X_R [a]	Percent error	$\Psi_R \times 10^3$ [a]	Percent error	C [a]	Percent error	$\tau_{xx,max}$ [b]	u_{max} [b]
0.0	1.5002	0.02	1.178	0.2	0.3741	0.1	–	1.501
0.1	1.499	0.2	1.169	0.5	0.310	0.3	0.349	1.495
0.2	1.499	0.2	1.169	0.4	0.259	0.3	0.367	1.483
0.5	1.518	0.3	1.236	0.2	0.188	0.4	0.393	1.457
1	1.579	0.2	1.513	0.7	0.171	0.6	0.400	1.453
2	1.732	0.3	2.345	1.4	0.201	0.8	0.373	1.461
5	1.988	0.2	3.302	0.8	0.288	0.5	0.285	1.472
10	2.017	0.2	2.162	0.6	0.352	0.3	0.206	1.478
20	1.854	0.1	0.935	0.5	0.388	0.4	0.138	1.484
50	1.579	0.3	0.303	1.0	0.398	0.1	0.0716	1.492
100	1.440	0.4	0.173	0.6	0.401	0.3	0.0415	1.496
1000	1.393	1.2	0.218	0.5	0.387	0.1	0.0071	1.500
10000	1.436	0.1	0.861	0.3	0.376	0.2	0.0011	1.501

[a] Based on the results obtained with meshes M2 and M4.
[b] Maximum values along centreline, normalised with $3\eta_0 U_2/H_2$ and U_2.

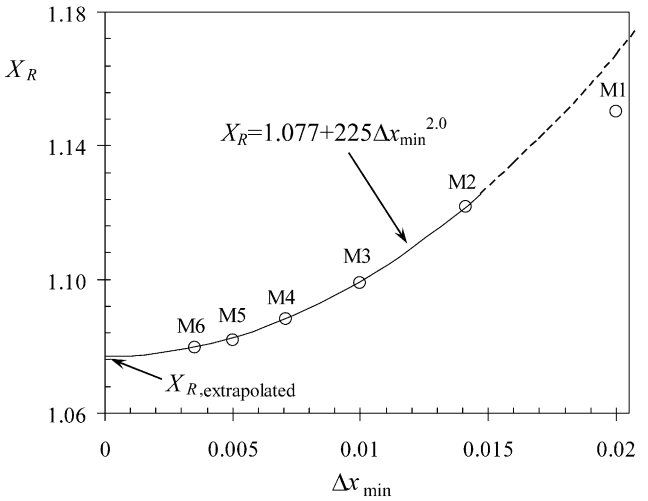

Fig. 6. Convergence of predicted vortex size (symbols) with mesh refinement for the Oldroyd-B fluid at $De = 2.5$.

of vortex size predicted on each mesh (M1–M6) are shown by the circles as a function of the minimum mesh spacing Δx_{min}, and the line represents a curve-fitting through the finest mesh values (M2–M6). It may be observed that the asymptotic range for the X_R variation is clearly achieved with the high degree of mesh refinement here applied, and the exponent of the mesh-size measure indicates the second-order accuracy expected from combination of a formally third-order scheme for the convection terms with a second-order scheme for the diffusion terms and the remaining approximations used in the discretisation.

In Fig. 7 the streamlines for the Oldroyd-B fluid, computed on the finest mesh M6, are presented. These show, qualitatively, shrinkage of the corner vortex with raising elasticity and the appearance of a small lip vortex at around $De \approx 1$. Although minute, the lip vortex is not an artifact of the computations: it is shown in Fig. 8 that its intensity is finite with extrapolation to a zero mesh size (recall that our mesh is very refined in the region around the re-entrant corner). From Fig. 8 it is also clear that, while for $De = 0.5$ and 1 the lip vortex vanishes when the grid resolution is infinitely increased, for $De = 1.5$ a finite lip vortex intensity remains when $\Delta x \to 0$. Such behaviour is more clearly shown in Fig. 9(a), where lip vortex streamlines are plotted over an enlarged local view of the various meshes, and in Fig. 9(b) where the asymptotic variation of lip vortex size and intensity with mesh fineness indicates finite values for zero mesh size. Note the linear convergence of the lip vortex characteristics, in contrast to the general quadratic convergence rate of the scheme; this is the best it can be achieved with such a small and localised flow feature as the lip vortex. Similar, but stronger, lip vortices were present in our previous simulations with the upper convected Maxwell model [6,12].

A view of the various stress component fields (τ_{xx}, τ_{yy}, τ_{xy}) and the pressure field in the entrance region is provided in Fig. 10. These predictions were obtained on the finest mesh M6 and correspond to the highest Deborah number achieved, $De = 2.5$. All fields are smooth, with highly localised stress concentration at the walls adjacent to the re-entrant corner. A more quantitative view of the local velocity and stress variations can be gained from asymptotic type of plots, which also serve to check some of the existing theories. These kinds of plots show radial profiles under log–log scales, emanating from re-entrant corner (distance r), at given angles θ measured anticlockwise from the incoming flow direction

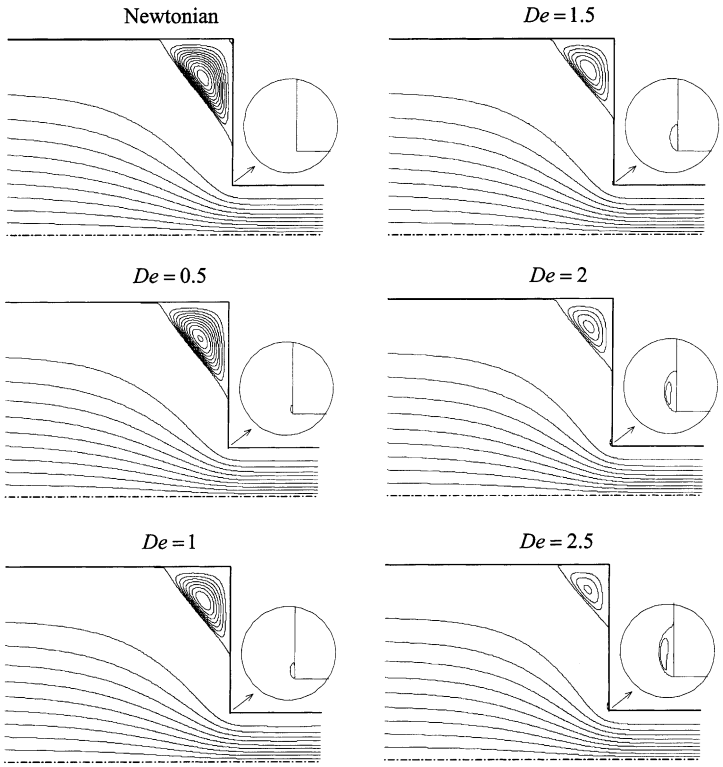

Fig. 7. Flow patterns with the Oldroyd-B fluid (mesh M6). Note: $\Delta\Psi_R = 0.1 \times 10^{-3}$ in recirculation.

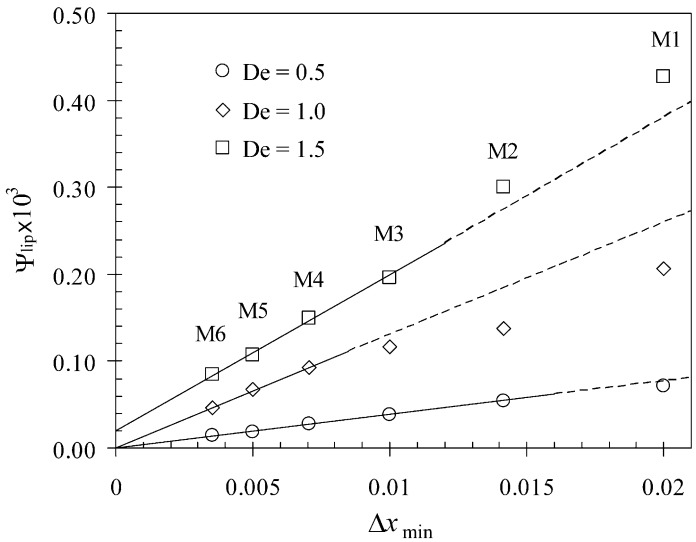

Fig. 8. Convergence with mesh refinement of the lip vortex intensity, for the Oldroyd-B fluid at Deborah numbers of 0.5, 1.0 and 1.5. Symbols are the predictions and lines the curve-fittings.

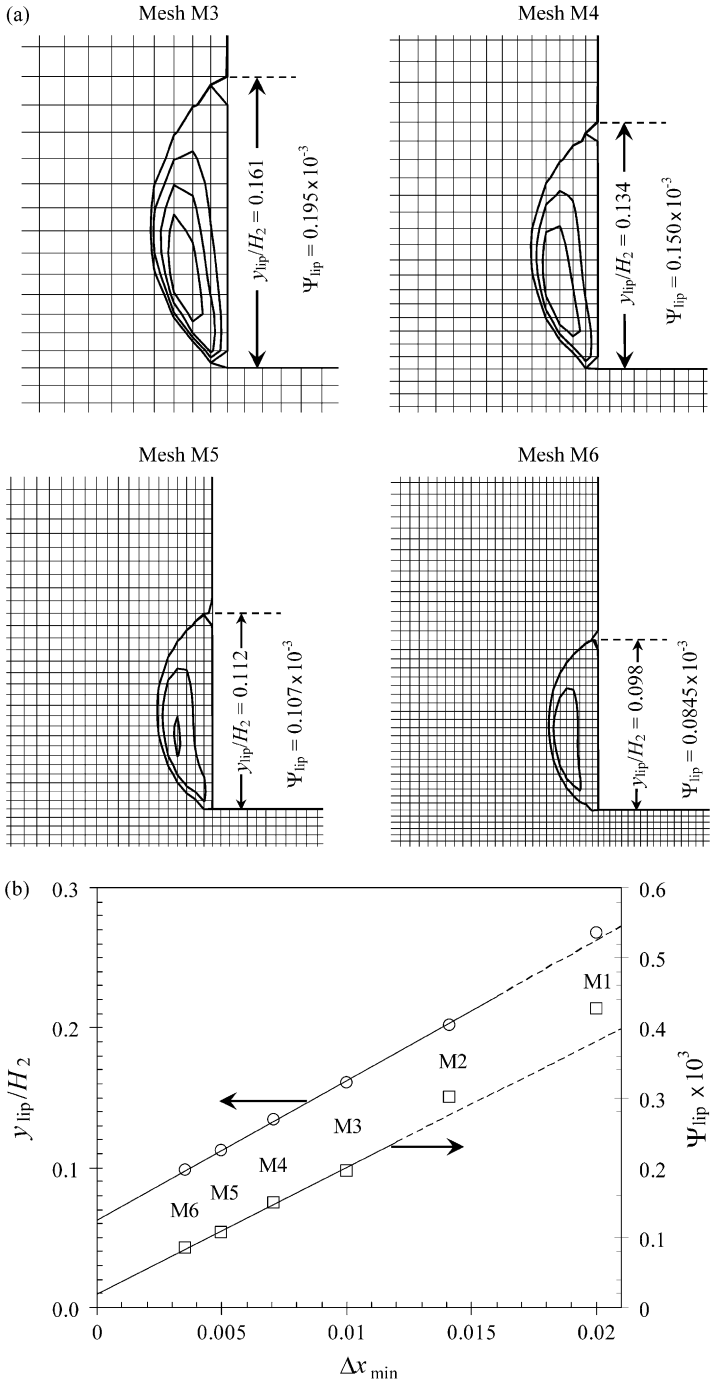

Fig. 9. Lip vortex for the Oldroyd-B fluid at $De = 1.5$. (a) Local view of streamlines and mesh. Note: in recirculation, $\Delta\Psi_L = 0.05 \times 10^{-3}$. (b) Variation of lip vortex size and strength with mesh refinement.

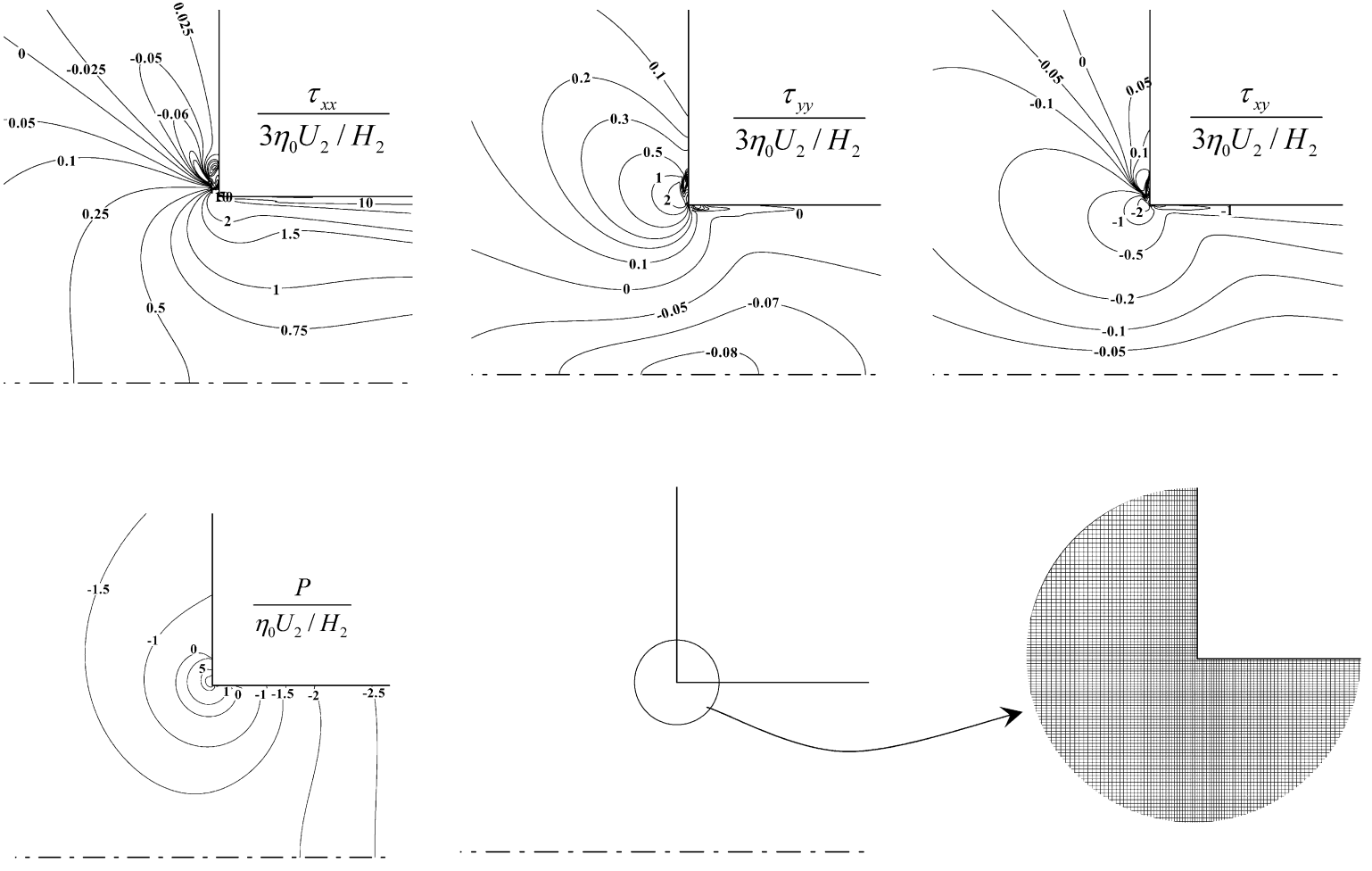

Fig. 10. Detail of the stress and pressure fields in a small region around the re-entrant corner, for the Oldroyd-B fluid at $De = 2.5$. Predictions on the finest mesh M6 (also shown).

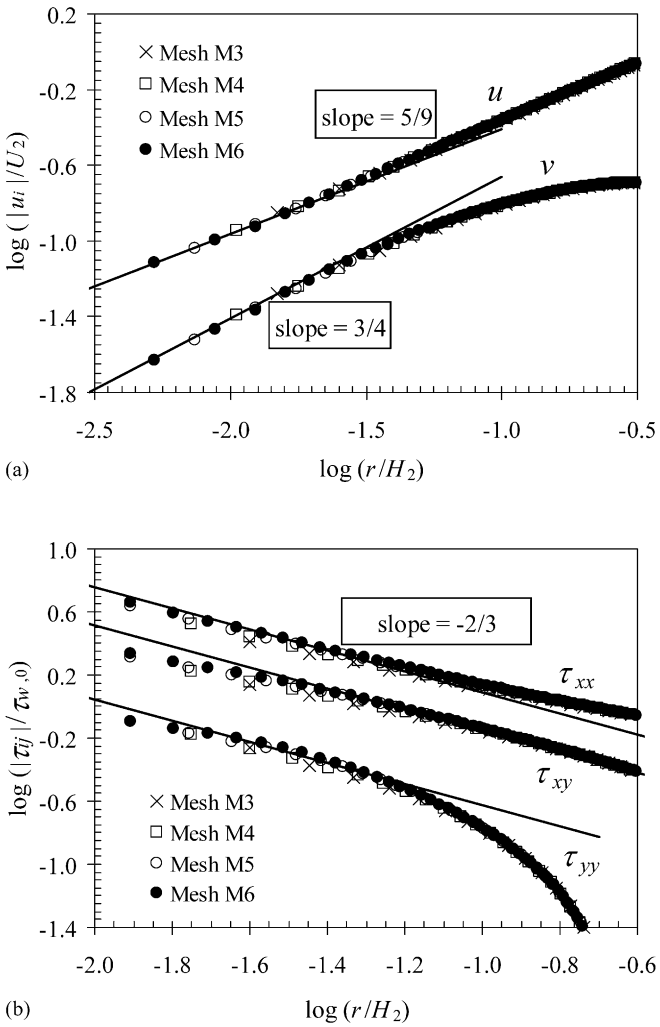

Fig. 11. Asymptotic variation near the re-entrant corner of (a) velocity and (b) stress components along a line at $\theta = 90^\circ$ (i.e. $x = 0$), for the Oldroyd-B fluid at $De = 1$.

(see Fig. 2). The most convenient angle is $\theta = 90^\circ$ which corresponds to profiles across the flow, along the Cartesian co-ordinate y, at $x = 0$; Fig. 11 shows such profiles on various meshes for the Oldroyd-B fluid at $De = 1$. This value of De was chosen to avoid the formation of a lip vortex which would violate the assumptions of the asymptotic theories (e.g. [19]). The predictions shown in Fig. 11 reveal good convergence when the computational meshes are refined, with the longitudinal and transversal velocity components going to zero near the corner as $r^{5/9}$ and $r^{3/4}$, respectively, and all three stress components going to infinity as $r^{-2/3}$; these slopes agree with the theory of Hinch [19]. Further study of the asymptotic behaviour of the UCM fluid (which essentially follows the Oldroyd-B behaviour) was given in a previous work [20], where both the Deborah number and the angle of the radial line were varied.

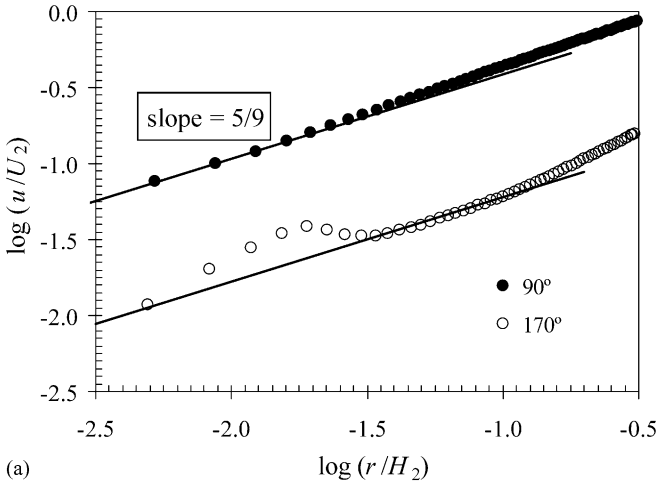

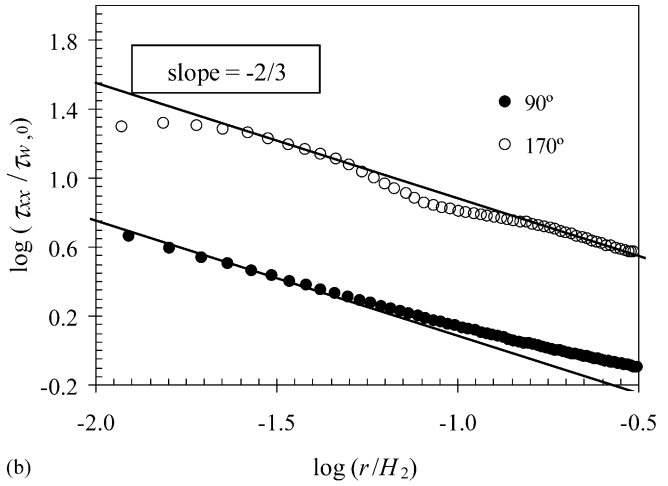

Fig. 12. Comparison of asymptotic variation for $\theta = 90^\circ$ (entrance to small channel, $x = 0$) and $\theta = 170^\circ$ (almost over downstream wall, $y/H_2 \cong 1$). Oldroyd-B fluid at $De = 1$ on mesh M6: (a) u-velocity component; (b) τ_{xx} stress component.

It is interesting here to compare the asymptotic variation along the $\theta = 90^\circ$ line with that at $\theta = 170^\circ$, a line almost coincident with the downstream channel wall. This is done in Fig. 12 and, although the perturbation near the singular point is higher for $\theta = 170^\circ$ than for $\theta = 90^\circ$, the slopes of the "radial" variation still seem to be $+5/9$ for the u-velocity and $-2/3$ for the τ_{xx} stress. Note that stress values exactly on the $\theta = 180^\circ$ line, that is over the downstream channel wall, are not actually calculated in our code but are only evaluated internally as boundary conditions to be applied to the momentum equations. In the next section, for the PTT fluid with the linear stress function, the behaviour close to the corner is studied in more detail.

Finally, we note that the Couette correction for the Oldroyd-B fluid decays linearly with De, as seen in Fig. 5, going to negative values in line with previous findings for the UCM; indeed, it would be unexpected

that a small amount of solvent viscosity would change the gross features of this flow. This linear variation can be accurately predicted with the correlation:

$$C = a - b\,De, \tag{10}$$

where $a = 0.4987$ and $b = 0.9983$ for $De \geq 1$ (regression factor of $R^2 = 0.99996$); for lower De the variation deviates slightly from a straight line but a good fit for all De is still obtained with $a = 0.4281$ and $b = 0.9665$ ($R^2 = 0.9991$). Pressure recovery at high elasticity can be attributed to the lack of dissipative effects in the Oldroyd-B model, but it is contrary to experimental observations. We may therefore conclude that both the UCM and Oldroyd-B equations are inadequate to model pressure drop through planar contractions, being unable to predict a localised (positive) loss coefficient. It is also true that experimentalists are at pain to measure accurate values for the loss coefficient, as illustrated by the recent work of Nigen and Walters [21], to which we shall come later when discussing pressure losses for the PTT model.

5. Results for the linear PTT fluid

This model is shear thinning on both the shear viscosity and the first normal stress difference coefficient. In addition, the elongational viscosity is limited, reaching a plateau at high strain rates, and the maximum value of the elongational viscosity varies inversely with the parameter ε. The first set of results to be presented corresponds to $\varepsilon = 0.25$, a typical value for the flow of concentrated polymer solutions and/or also for polymer melt flows.

Contrary to the Oldroyd-B fluid, both the size and intensity of the corner vortex for the linear PTT fluid are seen in Figs. 13 and 14 to increase monotonically with the Deborah number. Also, there is less sensitivity to mesh fineness, except possibly at high De, but not as noticeable as for the Oldroyd-B fluid. For purposes of benchmarking, all our results are tabulated in Table 3 with quantified uncertainties. For comparison, the data of Aboubacar et al. [8] are plotted in these figures; there is fair agreement, except for some erratic points. Notice also that the vortex recirculation tends to level out at high elasticity and so

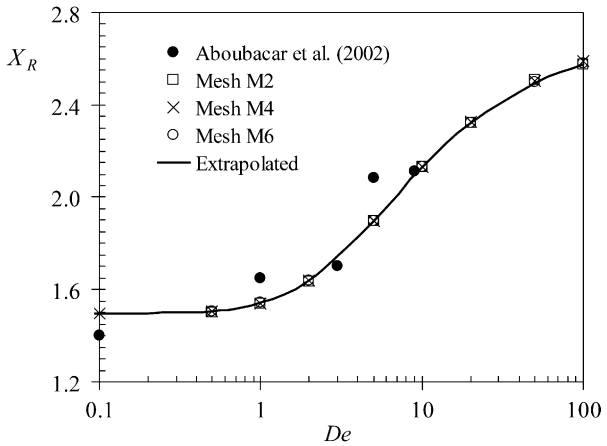

Fig. 13. Variation of the vortex size X_R with the Deborah number De (log scale) for the linear PTT fluid with $\varepsilon = 0.25$.

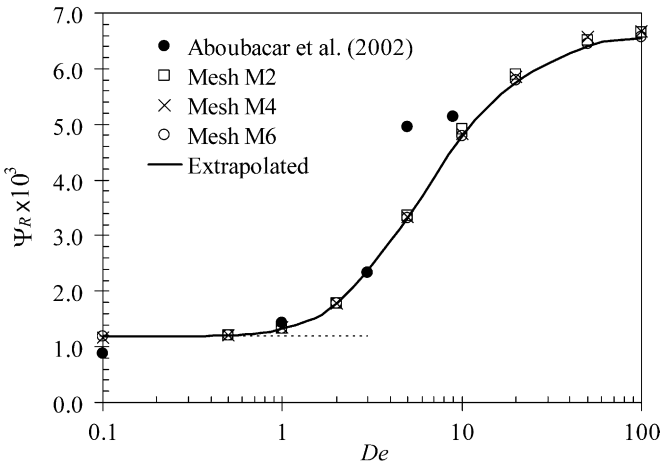

Fig. 14. Variation of the corner vortex intensity Ψ_R with the Deborah number *De* (log scale) for the linear PTT fluid with $\varepsilon = 0.25$.

the linear PTT model is not able to predict the very large corner vortices observed in some experimental visualisation works (see [21] and references therein).

The Couette correction results are given in Fig. 15 and the streamlines predicted on mesh M6 in Fig. 16. There is no sign of lip vortices for any of the *De* we have tried. The Couette correction *C* goes through a minimum, having a slightly negative value (elastic recovery), and is generally higher than that for the Oldroyd-B fluid, as shown under a linear *De* scaling in Fig. 17. A question arises: is the linear PTT model adequate to represent real fluid behaviour, namely in terms of entry losses? Possibly not, but the recent measurements of Nigen and Walters [21] for the planar contraction case are not conclusive. Looking at their Fig. 13 (syrup 2 and Boger fluid 2) we see a small pressure recovery which can be quantified as $C = -1.37$

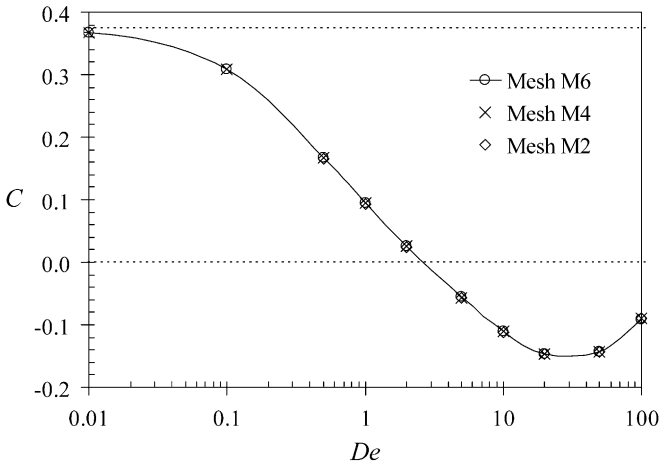

Fig. 15. Variation of the Couette correction *C* with the Deborah number *De* (log scale) for the linear PTT fluid with $\varepsilon = 0.25$.

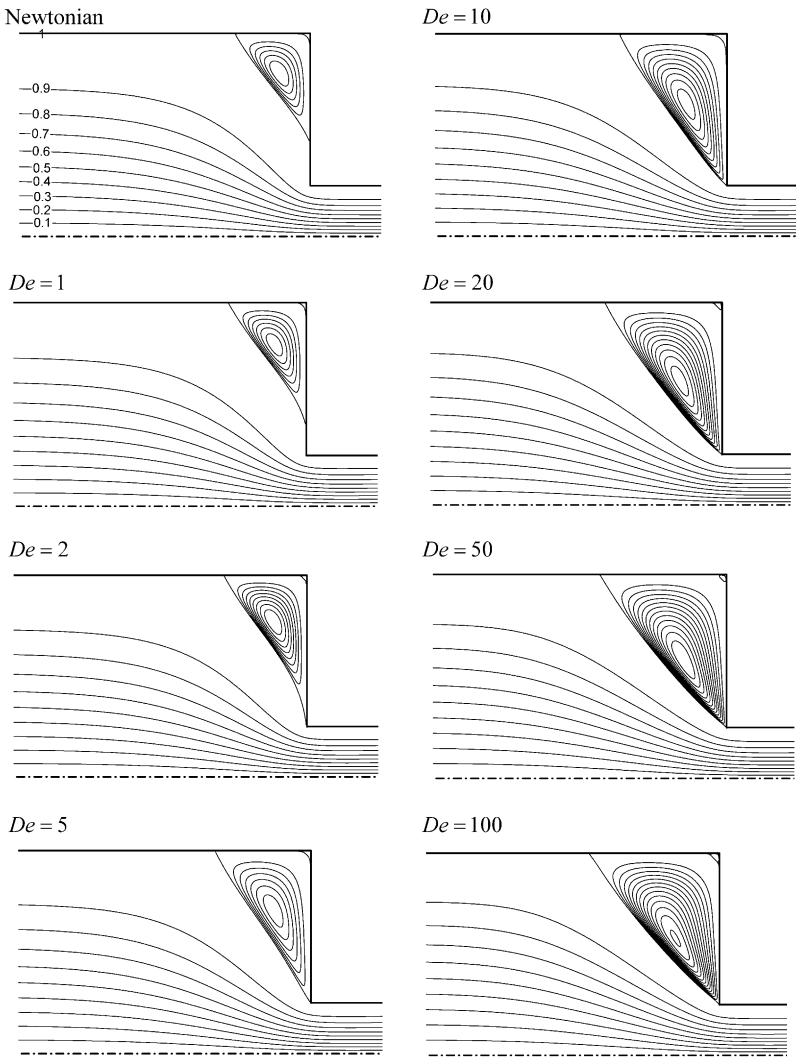

Fig. 16. Flow patterns with the linear PTT fluid ($\varepsilon = 0.25$, mesh M6). Note: in recirculation $\Delta\Psi_R = 0.2 \times 10^{-3}$ for $De \leq 2$; $\Delta\Psi_R = 0.5 \times 10^{-3}$ for $De \geq 5$.

for $Q = 40$ g/s. However, most probably this and other values of C, evaluated on the basis of the data measured by Nigen and Walters, are negative due to experimental uncertainties because their measurements for an axisymmetric contraction with a shorter outlet pipe clearly indicate a pressure loss ($C > 0$).

By employing a high degree of grid refinement in the region around the singular re-entrant corner we were able to study the asymptotic local variation of stresses and velocity, at distances increasingly closer to the corner (located at $x/H_2 = 0$ and $y/H_2 = 1$). The resulting variations along the radial line at an angle of 90° to the main flow direction are shown under log–log scales in Fig. 18, for the case $De = 1$. They follow power laws and are relatively smooth, with the velocity going to zero at a rate of 5/9, while the stresses go to infinity at a rate of −0.329. Such slopes for the asymptotic behaviour of the stress and

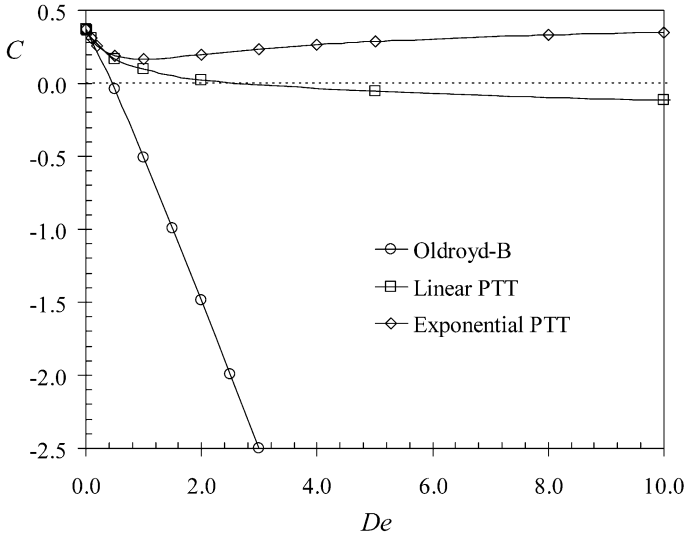

Fig. 17. Comparison of the predicted Couette correction for the Oldroyd-B and the PTT models.

velocity components near the corner closely match the theoretical derivation of Renardy [22] for the PTT fluid, and the local predicted variation is certainly more consistent than that in the recent results of Tanner et al. [23].

As done in the previous section for the Oldroyd-B fluid, it is interesting to compare here the asymptotic behaviour along two radial directions (Fig. 19, mesh M6): $\theta = 90^\circ$ (across the small channel entry, that is Cartesian direction at $x = 0$) and $\theta = 170^\circ$ (line almost over the small channel wall, that is $y \approx 1$). The predictions shown are for the case $De = 1$, and Fig. 19 clearly demonstrates that the rate of variation (measured by the slope of the straight lines passing through the data) remains the same for the two directions. For the profile along the line $\theta = 170^\circ$, it is, however, visible that the magnitude of the stress τ_{xx} is somewhat reduced in a few points very close to the singularity. In order to understand the stress behaviour near the singularity, we show in Fig. 20(a) axial profiles of the predicted τ_{xx} on the various meshes along the first row of cells adjacent to the downstream channel wall. With our cell-centred finite-volume scheme the values of τ_{xx} on the wall itself are not explicitly computed (in fact, they are not needed), and so it makes sense to use the closest available stresses which are directly computed on points internal to the computational domain.

There is good convergence with mesh refinement, except near the point of maximum τ_{xx} stress, which we shall denote as $\tau_{xx,\max}$ and $x(\tau_{xx,\max})$. Such a situation would be expected, since the more refined the mesh is, the higher stresses it will resolve near the singularity ($x = 0$, $y = 1$ under non-dimensional form); therefore, some localised region where convergence cannot be achieved will always exist. An asymptotic analysis of the variation of the maximum stress value and its location, as obtained on the various meshes, can provide us with valuable information. Fig. 20(b) shows how $\tau_{xx,\max}$ and the axial location where it occurs $x(\tau_{xx,\max})$ vary with the distance to the wall. These results demonstrate that $x(\tau_{xx,\max})$ converges linearly to the singular point ($x/H_2 = 0$, $y/H_2 = 1$; the re-entrant corner position) and that the rate of growth of the stress converges to -0.337 (with a correlation coefficient of $R = 0.99989$ for the power-law curve-fitting utilised). Hence, the asymptotic slope for the stress growth of Renardy's theory is reconfirmed by an alternative argument.

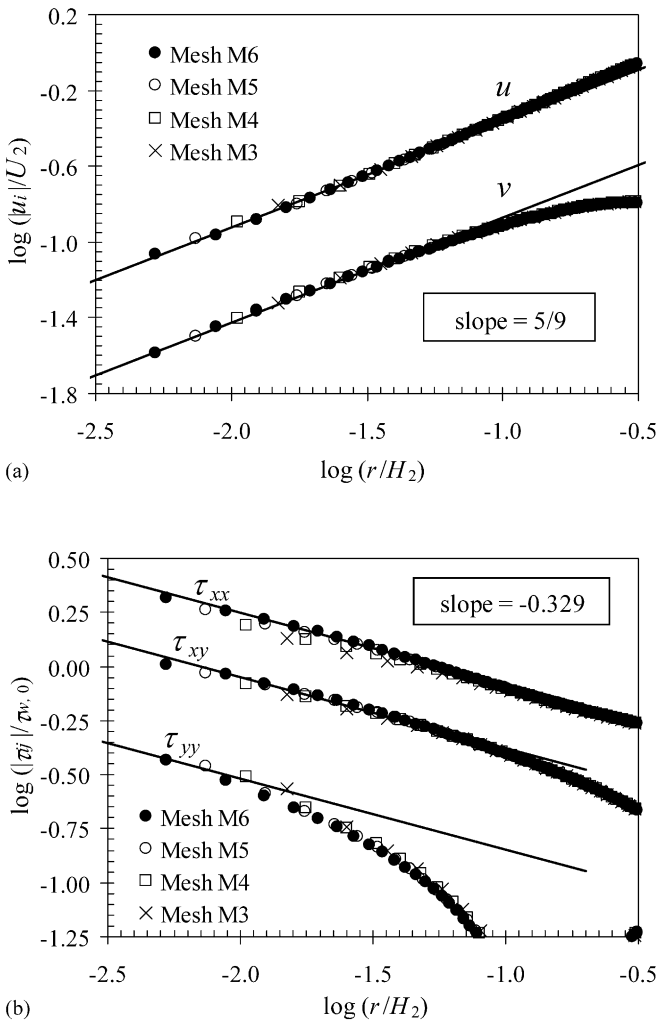

Fig. 18. Asymptotic behaviour near the re-entrant corner for the linear PTT fluid ($\varepsilon = 0.25$): (a) velocity; (b) stress.

In terms of local variations of the different fields (velocity, stress and pressure) all the computed results show smooth contour lines, with a concentration of stresses around the re-entrant corner and formation of stress boundary layers along the wall of the downstream channel. In order to present more quantitative results, we present in Figs. 21 and 22 longitudinal profiles along the centreline ($y = 0$) of the axial normal stress component (τ_{xx}) and the streamwise velocity component, for increasing level of elasticity, $De = 1$, 5, 10, 20, 50 and 100. In part (a) of these figures, a fixed scale is used to normalise the stress ($3\eta_0 U_2/H_2$) and the velocity (U_2); in part (b), the normalising stress is the fully developed shear stress at the wall for the PTT fluid ($\tau_{w,PTT}$) and the normalising velocity is the maximum centreline velocity for the PTT model under fully developed conditions. The purpose of such normalisation is to separate elastic/elongational effects from shear-thinning effects, as discussed hereafter.

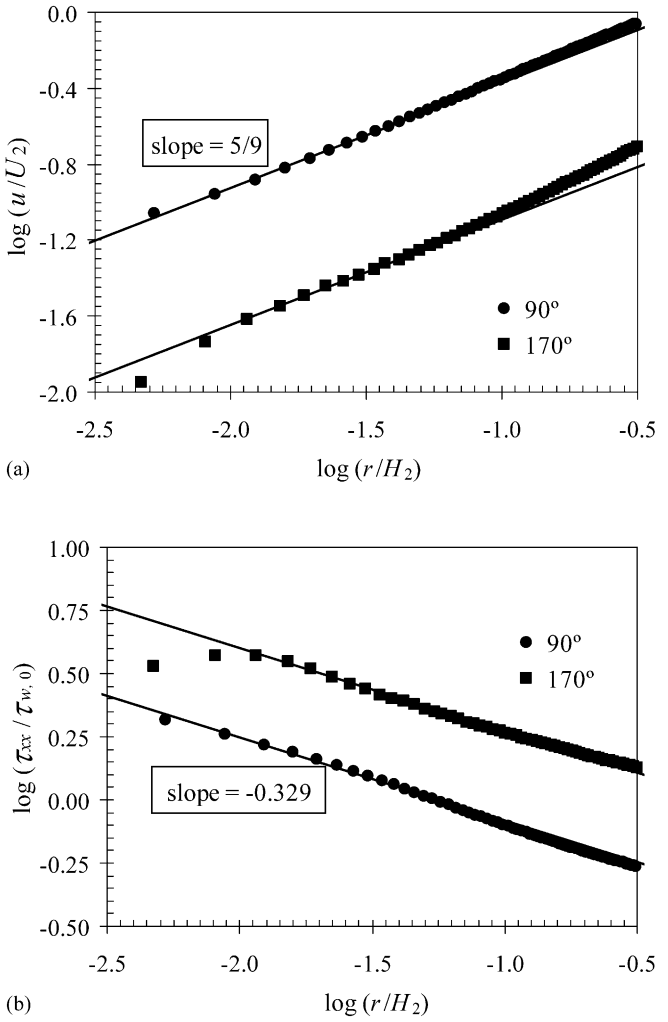

Fig. 19. Comparison of the asymptotic variation of (a) velocity and (b) normal stress along two radial lines: $\theta = 90^\circ$ and $\theta = 170^\circ$. Predictions on mesh M6 for the linear PTT model ($De = 1$).

In Fig. 21(a) the highest normal stress along the centreline is seen to occur further inside the smaller channel as *De* is increased, and its magnitude is seen to decrease with *De*. Since *De* is a measure of the elasticity in this fluid/flow configuration, one would expect to observe an increase in $\tau_{xx,\max}$ with elasticity; shear thinning is the only explanation for the decrease observed in Fig. 21(a). By scaling τ_{xx} with the wall shear stress of the PTT fluid itself, for each *De*, one seeks to remove a significant part of that shear-thinning effect and retain only the elastic effect. Fig. 21(b) shows that τ_{xx} scaled in this way exhibits increase with *De*, up to a level of $De \approx 20$; for higher *De*, $\tau_{xx,\max}$ tends to level out and decrease.

Such trend can be explained by examining the interrelated variations of elongational and shear characteristics in simple rheometric flows. Fig. 23(a) shows that the elongational viscosity $\eta_E(\dot{\varepsilon})$ for the linear PTT model with $\varepsilon = 0.25$ reaches a plateau at $\lambda\dot{\varepsilon} \approx 20$ and so elongational effects along the centreline of the contraction should come to an end at $De \approx 20$ (in this figure $\dot{\varepsilon}$ and $\dot{\gamma}$ are taken as equivalent). The

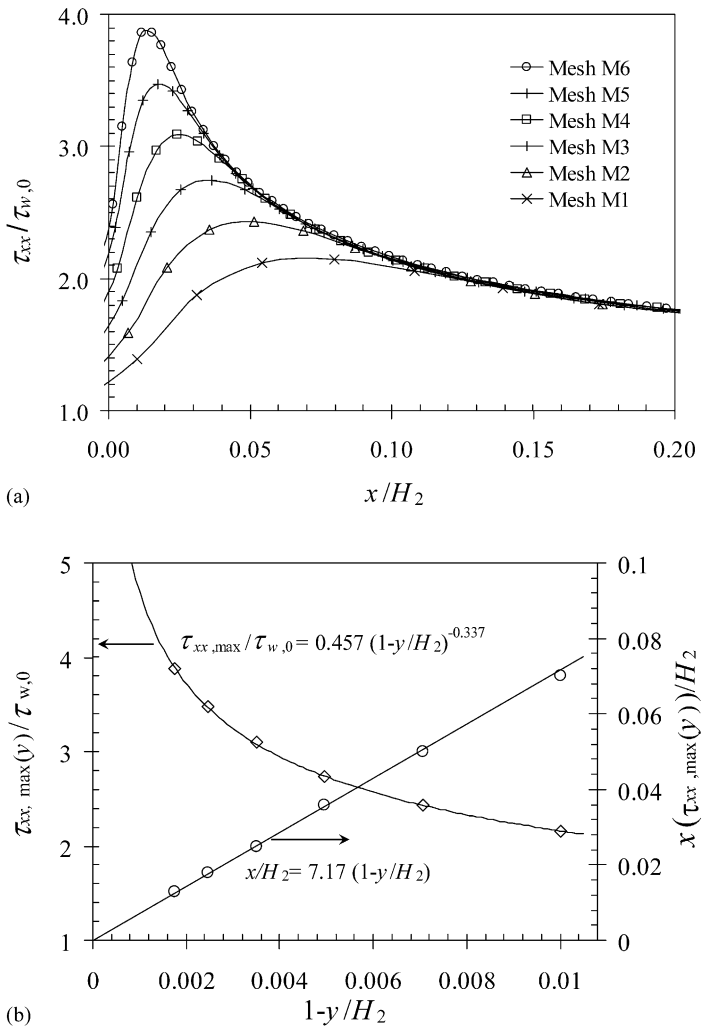

Fig. 20. Stress behaviour near the singularity for the linear PTT fluid at $De = 1$. (a) Variation of the predicted normal stress on various meshes along first row of cells adjacent to downstream channel wall. (b) Variation of the maximum value of the normal stress and its axial location, for each mesh, with distance to the wall. Best-fit correlations are also shown.

shear viscosity is however still decreasing at that range of $\lambda\dot{\gamma}$, albeit at a lower rate, hence the reduction in maximum τ_{xx}, seen in Fig. 21(b), and the velocity overshoot, seen in Fig. 22(b). Similar conclusions apply to the gradual stagnation of the rate of increase of Ψ_R and X_R seen in Figs. 13 and 14, respectively. An alternative explanation was given by Saramito and Piau [24] and later by Aboubacar et al. [8] who correlated the vortex patterns with the Trouton ration $T_R = \eta_E/\eta$ in simple extensional and shear flows. The rheometric data for the exponential PTT model is given in Fig. 23(b) thus highlighting the differences between the two forms of the PTT rheology.

A useful quantity one would like to know prior to carry out an actual simulation is the length of the outlet channel required for full redevelopment of the stresses, as that determines the size of the computational domain. From the creeping flow results obtained, it is clear that velocity develops very quickly, and the

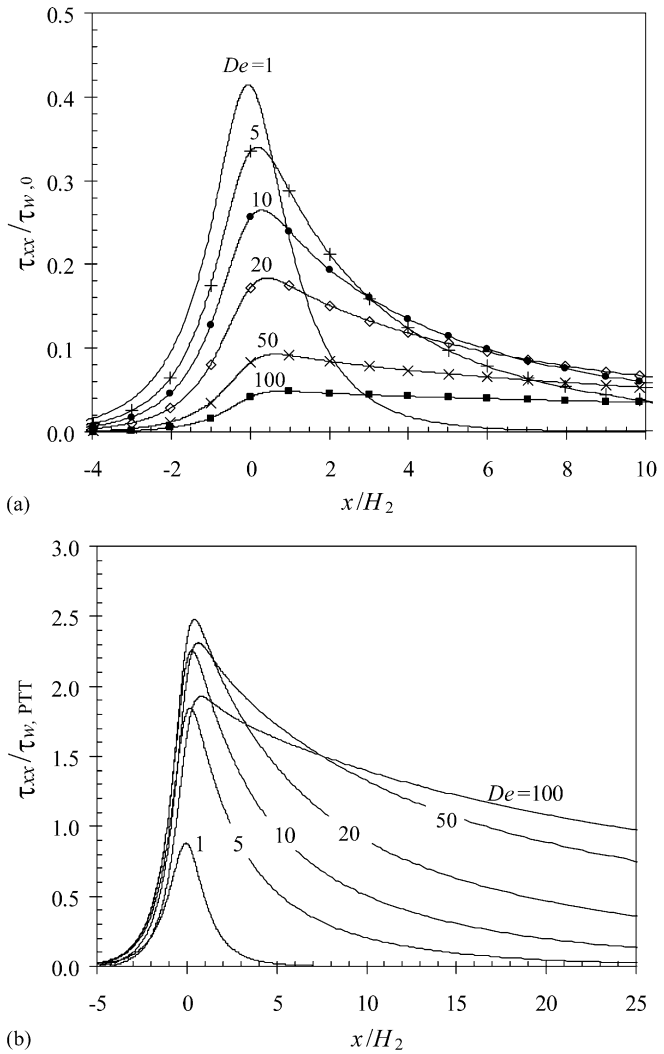

Fig. 21. Distribution of the axial normal stress τ_{xx} for the linear PTT model along the centreline: (a) scaled with $\tau_{w,0} = 3\eta_0 U_2/H_2$; (b) scaled with $\tau_{w,PTT}$.

slower stress component to relax to its fully developed state is the axial normal stress τ_{xx} acting along the centreline $y = 0$ of the contraction. In fact, the results show that τ_{xx} at the wall reaches its fully developed state much faster than at the centreline. For the purpose of predefining the computational domain, Fig. 24 presents the lengths (appropriately denoted $L_{\tau_{xx}}$) required for τ_{xx} to fall to either 1 or 5% of its maximum value along the centreline (which occurs by the contraction plane). These values of $L_{\tau_{xx}}$ evaluated on various meshes are seen to increase at a certain power of the Deborah number, tending towards direct proportionality of *De* as the computational mesh employed becomes sufficiently long and sufficiently refined. For the more precise criteria of 1%, we obtain the correlation:

$$\frac{L_{\tau_{xx}}}{H_2} \approx 4.3\,De, \tag{11}$$

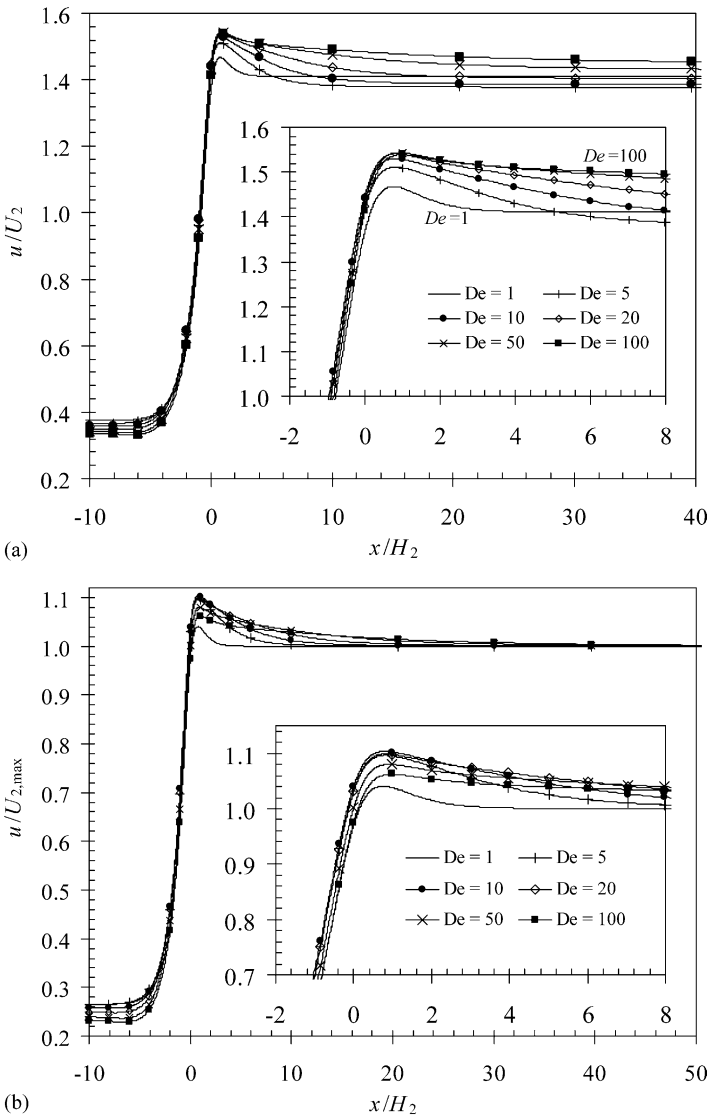

Fig. 22. Distribution of the axial velocity component u for the linear PTT model along the centreline: (a) scaled with U_2; (b) scaled with maximum velocity for the PTT under fully developed conditions.

showing that the computational domain must be $430H_2$ long when $De \approx 100$, while a length of $10H_2$ is adequate for $De = 1$–2. However, we emphasise again that the method utilised does not need a Dirichlet condition for stresses at outlet. In fact, the boundary condition applied is of the Neumann type ($\partial\tau_{ij}/\partial x = 0$) and thus may lead to some localised distortions for the low Reynolds number flows here considered ($Re = 0$); this type of error is not expected to affect the flow near the contraction, many channel-widths upstream. In any case, outlet channel lengths in agreement with Eq. (11) have been used in the actual computations so that the Couette corrections could be evaluated with high precision.

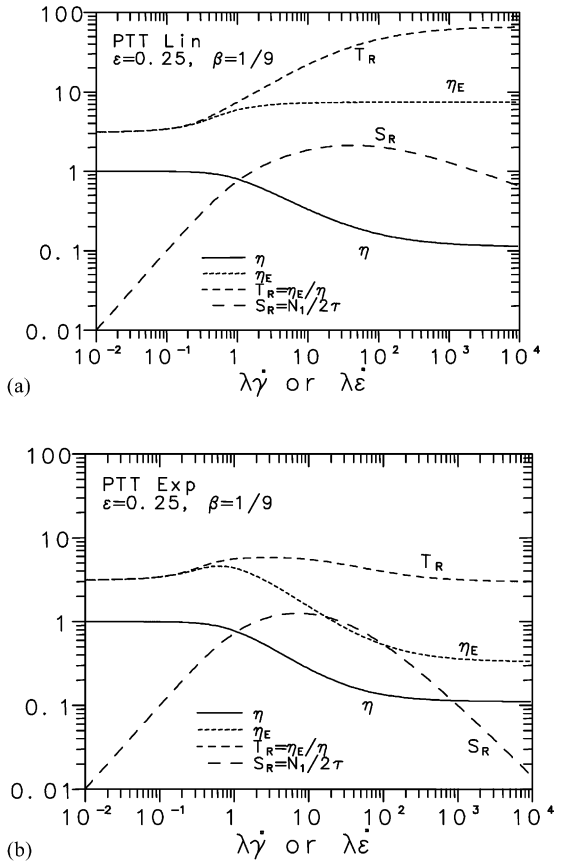

Fig. 23. Rheometric data of the PTT model with $\varepsilon = 0.25$: (a) linear; (b) exponential.

6. Results for the exponential PTT fluid

For the exponential form of the PTT fluid, the results of our calculations for $\varepsilon = 0.25$ are depicted in Fig. 25, giving X_R versus De; in Fig. 26, giving Ψ_R versus De; and in Fig. 27, giving C versus De; the corresponding numerical data are listed in Table 4. Again, fair agreement is seen with computations by Aboubacar et al. [8], except at $De = 0.1$ for the reasons noted above. The uncertainties in Table 4 are somewhat higher than in Table 3 because the runs here were based only on meshes M2 and M4, and not on M6; however, except for two values of the recirculation intensity at $De = 100$ and 1000, the uncertainty is generally below 1%. In these runs, it was important to use an extended length for the downstream channel as De was increased, according to the estimate given by Eq. (11); otherwise, the discrepancy between results on meshes M2 and M4 would be visible in the figures. M4 was deemed adequate for this fluid case; runs at $De = 1$ and 100 on meshes M4 and M6 showed a difference in X_R below 0.1 and 0.5% for Ψ_R.

In these simulations, the Deborah number was varied all the way from $De = 0$, the Newtonian case, to the extremely high value of $De = 10{,}000$, when shear thinning becomes so strong that the apparent

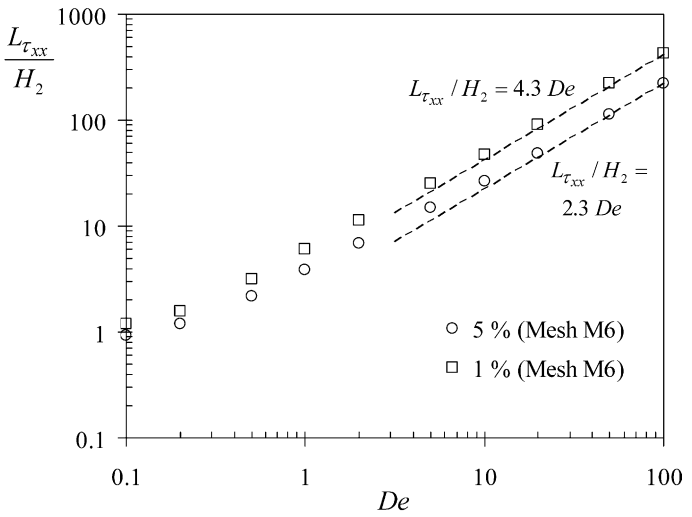

Fig. 24. Length required for relaxation of the normal stress as a function of the Deborah number (linear PTT, $\varepsilon = 0.25$).

viscosity is effectively reduced back to the level of the Newtonian solvent value. So, it is not surprising to see that both the corner vortex size and its strength go through an initial maximum, at $De \approx 6$–7 when the Trouton ratio T_R and the recoverable stress S_R peak (cf. Fig. 23), followed by a reduction to levels below those of the Newtonian case and then, as De is further increased, they tend asymptotically to the Newtonian values from below. There is thus confirmation that the predicted flow features are again Newtonian-like at very high Deborah numbers. The fact that both Ψ_R and X_R are smaller than the Newtonian values at an intermediate De range is plausible, just as happened for the Oldroyd-B fluid. For example, Saramito and Piau [24] (their Fig. 11b) and Aboubacar et al. [8] (their Figs. 14, 16 and 20) have also found vortex intensities below the Newtonian values, with exponential versions of the PTT fluid. Also, there is evidence of a very slight influence of mesh refinement, somewhat more accentuated for

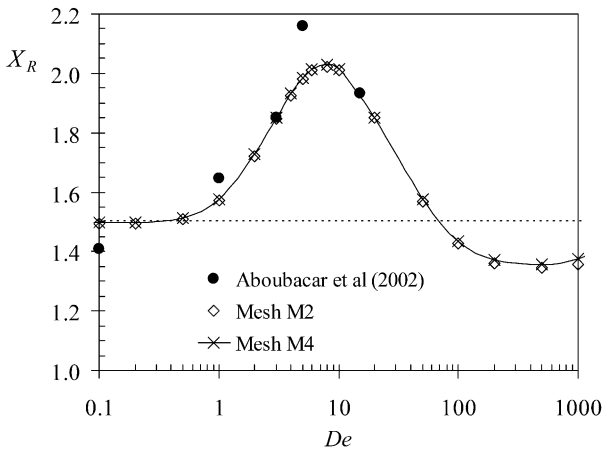

Fig. 25. Variation of the vortex size X_R with the Deborah number De (log scale) for the exponential PTT fluid with $\varepsilon = 0.25$.

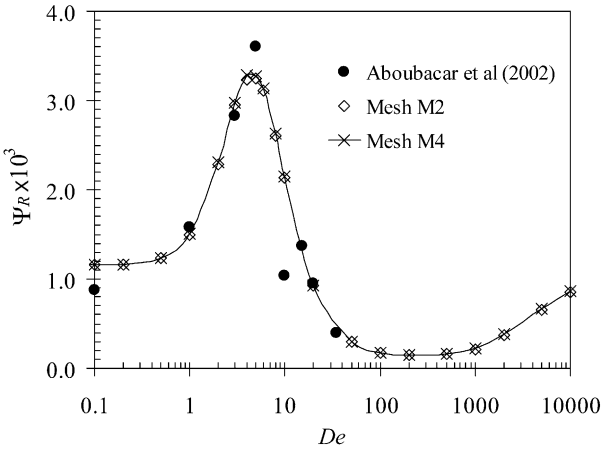

Fig. 26. Variation of the corner vortex intensity Ψ_R with the Deborah number *De* (log scale) for the exponential PTT fluid with $\varepsilon = 0.25$.

X_R at $De \approx 1000$ (difference of 1.2% between results on meshes M2 and M4), but otherwise it has been confirmed that mesh M4 is adequate to accurately resolve the main flow features. It should also be clear from Fig. 24 that very long outlet (and also inlet) channel lengths were employed in order to keep the solution accuracy within reasonable bounds (the longest lengths were $L_1 = 500H_2$ and $L_2 = 1500H_2$, for $De = 10{,}000$).

As found previously by Keunings and Crochet [25] and Saramito and Piau [24] (although both these studies were for axisymmetric contractions), and by Aboubacar et al. [8], the Couette correction for this rheological model goes through a minimum at low *De*, and then increases when *De* is further increased, more in line with experimental observations. However, real fluids tend to show much higher values of localised pressure losses (that is, of Couette correction factor *C*). It is important to note that the wall shear stress τ_w used for the normalisation of the pressure drop in the definition of Couette correction is

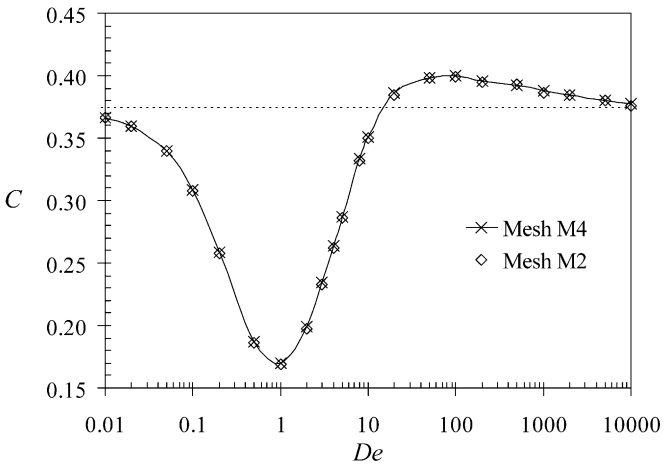

Fig. 27. Variation of the Couette correction *C* with the Deborah number *De* (log scale) for the exponential PTT fluid with $\varepsilon = 0.25$.

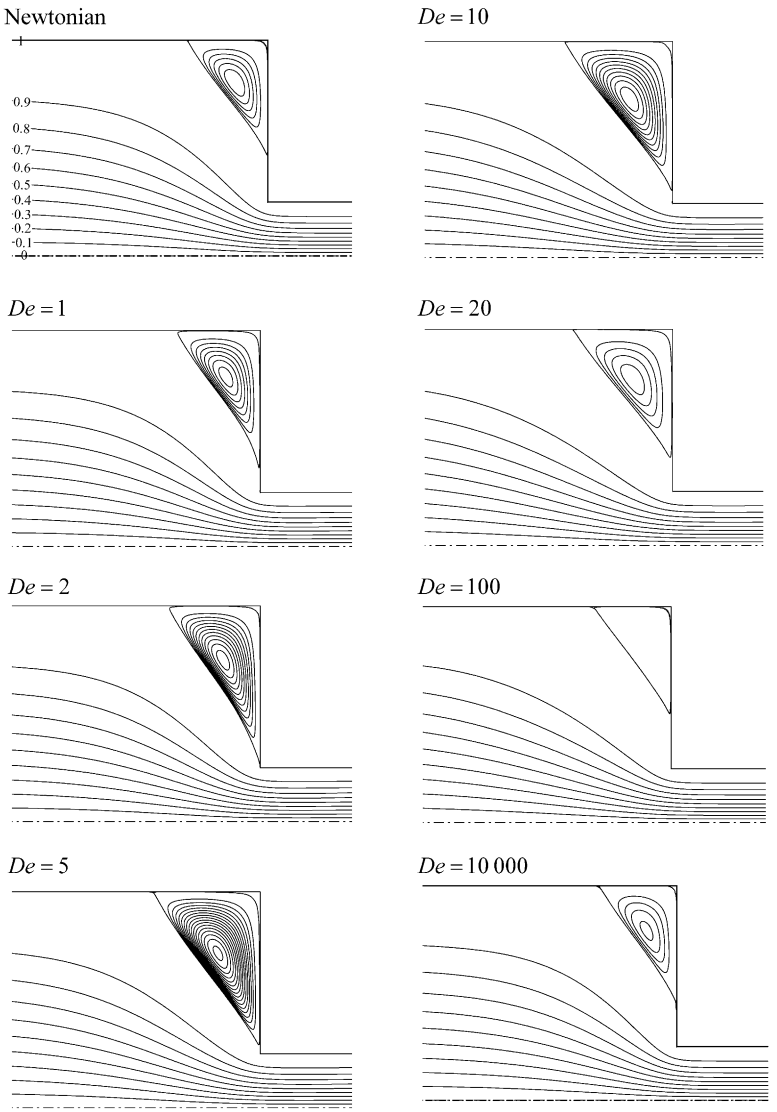

Fig. 28. Predicted flow patterns with the exponential PTT fluid ($\varepsilon = 0.25$, mesh M4). Note: $\Delta\Psi_R = 0.2 \times 10^{-3}$ in recirculation.

the actual fully developed stress at the wall for the exponential form of the PTT model (including the Newtonian contribution from the solvent stress). Its values were evaluated from the simulation results and could be approximately checked with the analytical solution of Oliveira and Pinho [26], valid for the situation without a solvent viscosity. For example, at low *De*, when the solvent viscosity may be discarded, the analytical solution gives $\tau_w = 0.975$ ($De = 0.1$) and $\tau_w = 0.913$ ($De = 0.2$), while the computations gave, respectively, $\tau_w = 0.977$ and $\tau_w = 0.923$. At high *De*, when the 1/9 contribution from the solvent should be added to the analytical solution, this yields $\tau_w = 0.267$ for $De = 5$ (computations $\tau_w = 0.264$) and $\tau_w = 0.199$ for $De = 10$ (computations $\tau_w = 0.200$), thus demonstrating the correctness of the computed wall shear stress. Since this τ_w shows a significant decrease with *De* on account of shear

thinning, part of the rise of C (see also Fig. 17) can be attributed to the influence of the scaling employed to non-dimensionalise the pressure decrease.

The flow patterns for the exponential PTT are given in Fig. 28, to be compared with the streamlines of Fig. 16 for the linear version of the PTT. Although the stream-function spacing inside the recirculation is not exactly the same in both figures, it is clear that the exponential form exhibits smaller vortices with less quantity of recirculating fluid. It may be concluded, based on the variations of Fig. 23, that these features are related to either the levelling out and reduction of extensional viscosity at high strain rates or the variation of the recoverable stress ratio.

7. Conclusions

The main purpose of the work was to give sufficiently accurate results for the vortex size and intensity, and for the pressure loss, in planar contraction flows with a 4:1 cross-section area ratio, of Oldroyd-B and PTT fluids with a solvent viscosity ratio of $\eta_s/\eta_0 = 1/9$. These data are given in Tables 2–4, where the corresponding uncertainty is quantified. We expect that these extrapolated data, based on calculations on very fine meshes, may be useful for other authors in validation/demonstration works. It is fair to note that no data of similar quality existed previously to the present undertaking, in spite of the viscoelastic flow through a planar contraction being accepted as a test case since 1988 [1]. Finally, no upper limit on De was found for the exponential form of the PTT constitutive model, while an approximate limit of $De \approx 200$ was found for the linear form, in contrast to maximum Deborah numbers of 9, for the linear PTT, and 35, for the exponential PTT, found in [8].

All the computations have been carried out with a finite-volume method on very refined meshes, with over 1 million degrees of freedom, and the spatial discretisation was based on a purpose-built high-resolution scheme guaranteeing second-order accuracy and good iterative convergence properties. Extreme care was exercised throughout this numerical study to guarantee that the results obtained were accurate, and that their accuracy was reliably quantified. We hope the results may be useful for other workers in the field.

Acknowledgements

M.A. Alves wishes to thank Universidade do Porto and his colleagues at Departamento de Engenharia Química, FEUP, for a temporary leave of absence. He also wishes to acknowledge the financial support provided by Fundação Calouste Gulbenkian.

References

[1] O. Hassager, Working Group on Numerical Techniques, in: Proceedings of the Vth Workshop on Numerical Methods in Non-Newtonian Flow, J. Non-Newtonian Fluid Mech. 29 (1988) 2–5.

[2] R.A. Brown, G.H. McKinley, Report on VIIIth International Workshop on Numerical Methods in Viscoelastic Flows, J. Non-Newtonian Fluid Mech. 52 (1994) 407–413.

[3] Y. Fan, R.I. Tanner, N. Phan-Thien, Galerkin/least square finite-element methods for steady viscoelastic flows, J. Non-Newtonian Fluid Mech. 84 (1999) 233–256.

[4] M.A. Alves, F.T. Pinho, P.J. Oliveira, The flow of viscoelastic fluids past a cylinder: finite-volume high-resolution methods, J. Non-Newtonian Fluid Mech. 97 (2001) 207–232.
[5] T.N. Phillips, A.J. Williams, Viscoelastic flow through a planar contraction using a semi-Lagrangian finite volume method, J. Non-Newtonian Fluid Mech. 87 (1999) 215–246.
[6] M.A. Alves, F.T. Pinho, P.J. Oliveira, Effect of a high-resolution differencing scheme on finite-volume predictions of viscoelastic flows, J. Non-Newtonian Fluid Mech. 93 (2000) 287–314.
[7] M. Aboubacar, M.F. Webster, A cell-vertex finite volume/element method on triangles for abrupt contraction viscoelastic flows, J. Non-Newtonian Fluid Mech. 98 (2001) 83–106.
[8] M. Aboubacar, H. Matallah, M.F. Webster, Highly elastic solutions for Oldroyd-B and Phan-Thien/Tanner fluids with a finite volume/element method: planar contraction flows, J. Non-Newtonian Fluid Mech. 103 (2002) 65–103.
[9] R. Ahmed, R.F. Liang, M.R. Mackley, The experimental observation and numerical prediction of planar entry flow and die swell for molten polyethylenes, J. Non-Newtonian Fluid Mech. 59 (1995) 129–153.
[10] L.M. Quinzani, R.C. Armstrong, R.A. Brown, Use of coupled birefringence and LDV studies of flow through a planar contraction to test constitutive equations for concentrated polymer solutions, J. Rheol. 39 (1995) 1201–1228.
[11] F. Legrand, J.M. Piau, Spatially resolved stress birefringence and flow visualization in flow instabilities of a polydimethylsiloxane extruded through a slit die, J. Non-Newtonian Fluid Mech. 77 (1998) 123–150.
[12] P.J. Oliveira, F.T. Pinho, Plane contraction flows of upper convected Maxwell and Phan-Thien/Tanner fluids as predicted by a finite-volume method, J. Non-Newtonian Fluid Mech. 88 (1999) 63–88.
[13] N. Phan-Thien, R.I. Tanner, A new constitutive equation derived from network theory, J. Non-Newtonian Fluid Mech. 2 (1977) 353–365.
[14] N. Phan-Thien, A nonlinear network viscoelastic model, J. Rheol. 22 (1978) 259–283.
[15] P.J. Oliveira, F.T. Pinho, G.A. Pinto, Numerical simulation of non-linear elastic flows with a general collocated finite-volume method, J. Non-Newtonian Fluid Mech. 79 (1998) 1–43.
[16] M.A. Alves, P.J. Oliveira, F.T. Pinho, A convergent and universally bounded interpolation scheme for the treatment of advection, Int. J. Numer. Meth. Fluids 41 (2003) 47–75.
[17] P.H. Gaskell, A.K.C. Lau, Curvature-compensated convective transport: SMART, a new boundedness preserving transport algorithm, Int. J. Numer. Meth. Fluids 8 (1988) 617–641.
[18] M.A. Rogerson, Y.L. Yeow, Representation of Stokes flow through a planar contraction by Papkovich–Fadle eigenfunctions, J. Appl. Mech. 66 (1999) 940–944.
[19] E.J. Hinch, The flow of an Oldroyd-B fluid around a sharp corner, J. Non-Newtonian Fluid Mech. 50 (1993) 161–171.
[20] M.A. Alves, P.J. Oliveira, F.T. Pinho, Numerical simulations of viscoelastic flow around sharp corners, in: Computational Fluid and Solid Mechanics, Elsevier, Amsterdam, 2001, pp. 772–775.
[21] S. Nigen, K. Walters, Viscoelastic contraction flows: comparison of axisymmetric and planar configurations, J. Non-Newtonian Fluid Mech. 102 (2002) 343–359.
[22] M. Renardy, Re-entrant corner behavior of the PTT fluid, J. Non-Newtonian Fluid Mech. 69 (1997) 99–104.
[23] R.I. Tanner, A. Jabbarzadeh, S.-C. Xue, Computations at sharp corners, in: proceedings of the XIIIth International Congress on Rheology, vol. 2, Cambridge, 2000, pp. 181–183.
[24] P. Saramito, J.M. Piau, Flow characteristics of viscoelastic fluids in an abrupt contraction by using numerical modeling, J. Non-Newtonian Fluid Mech. 52 (1994) 263–288.
[25] R. Keunings, M.J. Crochet, Numerical simulation of the flow of a viscoelastic fluid through an abrupt contraction, J. Non-Newtonian Fluid Mech. 14 (1984) 279–299.
[26] P.J. Oliveira, F.T. Pinho, Analytical solution for fully developed channel and pipe flow of Phan-Thien–Tanner fluids, J. Fluid Mech. 387 (1999) 271–280.